


**Spin-thermoelectric transport in nonuniform strained zigzag graphene nanoribbons**Fereshte Ildarabadi and Rouhollah Farghadan \**Department of Physics, University of Kashan, Kashan 87317-53153, Iran* (Received 25 December 2020; revised 14 February 2021; accepted 4 March 2021; published 16 March 2021)

We study a nonuniform strain in zigzag graphene nanoribbons for producing the spin-thermoelectric effects, using the mean-field Hubbard approximation and a Green's function approach. Our theoretical results show that a sinusoidal-shaped inhomogeneous strain with electron-electron interaction could induce a different effect on each edge of zigzag nanoribbons and finally generate a spin semiconductor with a tunable spin-dependent band gap. The strength of strain also controls the magnitude of magnetization in each edge. Interestingly, pure spin current and a giant spin Seebeck coefficient can be produced even at low values of strain by applying a thermal gradient and without magnetic elements. These results pave a practical way toward improved design for spin-thermoelectric applications through strain engineering.

DOI: [10.1103/PhysRevB.103.115424](https://doi.org/10.1103/PhysRevB.103.115424)**I. INTRODUCTION**

Strain as a possible effective way to tailor electronic properties of two-dimensional materials has been studied significantly [1–6]. Strain induces new features via changing atomic bond length, angle, and strength [7]. Experimentally, some methods to induce strain in 2D materials are epitaxial interaction, thermal expansion mismatch, patterning substrates, and stretching of flexible substrates [8,9]. Substrate surface topography modification and piezoelectric substrate actuation are also used to apply strain in the sample [7].

Graphene is verified to be one of the most persistent 2D materials exposed to strain [10]. Its unit cell can endure elastic tensile strain more than 20% without breaking [10]. Thus, graphene is a feasible candidate for straintronics [4,11–13] due to its high mechanical stability [10].

Based on previous studies, inducing strain in graphene gives rise to producing an effective scalar potential [14] and a useful gauge potential in the system [15,16]. The induced pseudomagnetic field has opposite signs for two valleys, while the external magnetic field has the same effect on all electrons in the lattice [8]. Also, an in-plane electric field may be generated in regions with different stretches due to the various local electron densities [8]. Strain by changing the features of the Dirac fermions reveals new fascinating transport properties. For instance, the Dirac cones are shifted away from previous positions by uniaxial strain below the critical strain value in graphene around 20% and become massive in strain values above the critical value [17,18]. Opening a band gap by uniaxial strain has been studied a lot in graphene [19,20]. Contrarily, biaxial strain only changes the Fermi velocity by varying the slope of the Dirac cones [17]. Moreover, some strain distributions by inducing strong uniform pseudomagnetic field give rise to the appearance of

a pseudo-quantum-Hall effect in the absence of real magnetic field [4,21,22].

Changing the spin polarization and the local magnetization is another exciting performance of strained graphene [21,23–25] for spintronic devices. Enhancing the magnetic order at edges of graphene nanoribbons (GNRs) and quantum dots was predicted by Viana-Gomes *et al.* [26]. Then it was extensively studied, and we mention some of the studies here. Lu and Guo indicated that strain changes the spin polarization at the edges of GNRs in the presence of the Hubbard interaction and, in addition to that, adjusts the band gap [19]. Kou *et al.* revealed a ferromagnetic ground state for strained graphene with line defects [24]. Inducing a magnetic effect in rippled graphene by vacancies is also explored in [23]. Chang *et al.* assumed an arc-bend strained GNR with Hubbard repulsion and showed that a measurable polarization difference between two sublattices is induced and generates nonuniform magnetic field [21]. In addition, Yang *et al.* illustrated that Coulomb interaction induces a ferromagnetic-like behavior under a proper strain, and strain could control graphene magnetism [27]. Other researchers investigated edge magnetism of graphene quantum dots [28,29] and spin-resolved transport of strained with external exchange field [30]. Recently, transistors using strained graphene have been introduced too [31].

On the other hand, strain increases the mismatch between phonon vibrations, leading to suppressing thermal conductivity [32,33]. Hence, the strained graphene could be a good choice for devices with thermal transport. Thermal conductivity of both strained and unstrained graphene sheets [33] and graphene nanoribbons [34] has been calculated. Moreover, the band gap opened in graphene by strain, owing to the modified orbital hybridization [35,36], has added another superiority for graphene-based thermoelectric devices. First-principles studies investigated the thermoelectric properties of strained graphene nanoribbons [37]. Mani and Benjamin also showed that strained graphene acts as a highly efficient quantum heat engine operating at maximum power [38,39]. Also, thermal

\*rfarghadan@kashanu.ac.ir

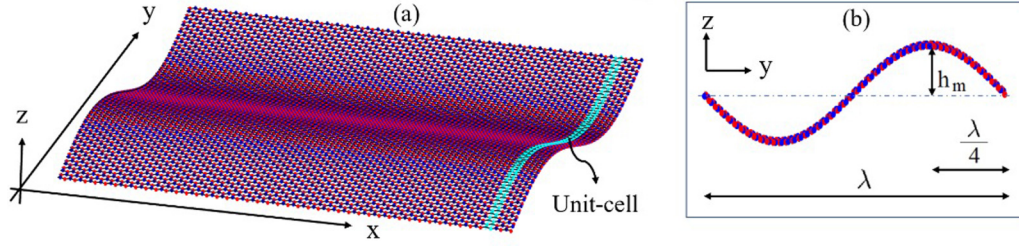


FIG. 1. Sinusoidal strain applied along the width of ZGNR.  $\lambda$  and  $h_m$  denote the wavelength and amplitude of the wave, respectively. The periodic structure of the ZGNR is along the  $x$  axis, and the sinusoidal strain is extended in the  $y$  direction perpendicular to the nanoribbon.

transport in the strain-induced rippled graphene is studied in Ref. [40].

Very recently, Banerjee *et al.* disused a periodic strain on a graphene sheet that created a strong periodic pseudo-gauge-field varying at the sample's length scale and studied its Dirac behavior electrons [8]. The inhomogeneous strain gradient creates nonuniform pseudomagnetic and electric fields resulting in new transport properties [8]. Furthermore, electronic properties of rippled graphene are affected by height, wavelength, and a number of these deformations [8,41]. Ripples are also detected in suspended graphene, in addition to graphene on a substrate [42]. However, several theoretical proposals on various shapes of rippled graphene and experimental attempts have been performed that achieved exotic findings which can be found in [43–47].

Our idea in this work is assuming a sinusoidal (strain based on [8]) transverse to a zigzag graphene nanoribbon (ZGNR) in the presence of e-e interaction. Our choice is due to the magnetic features of the zigzag edge GNRs contrary to the armchair GNRs [48]. Then we apply the temperature gradient nanoribbon. This nonuniform strain induces different hopping amplitudes across the ribbon resulting in impressive band structure beside the Hubbard interaction. The presence of Hubbard interaction causes local magnetism resulting in strong spin polarization. Consequently, applying a temperature gradient could make a pure thermospin current and large Seebeck effect. The proposed system could be a practical candidate for new transport device generation through strain engineering.

## II. METHOD

We applied a sinusoidal strain with out-of-plane displacements along the width of the ZGNR as depicted in Fig. 1. Dislocation of each atom in the strained ZGNR (SZGNR) relative to its position in the ZGNR is determined by  $h(y) = h_m \sin(2\pi y/\lambda)$  with  $\lambda$  and  $h_m$  being the wavelength and amplitude of the sinusoidal function, respectively. This shape of strain has been introduced on the graphene sheet by Banerjee *et al.* in [8] along with an in-plane displacement. Here, we consider zero in-plane stretchings, while all atoms in a specific  $y$  are displaced in the  $z$  direction by the value  $h(y)$ . In the presence of such strain, the carbon-carbon bond length around the peaks of the sinusoid is shorter compared with middle locations. It is worth noting that such a nonlinear out-of-plane strain profile can be rescaled to an in-plane strain tensor by the Foppl-von Karman model [49,50]. Especially, when

our out-of-plane sinusoidal strain wavelength is very large analogously to the atomic bond length, the in-plane strain approximation by the Foppl-von Karman model is extremely close to our strain profile in every point of the ribbon. The accuracy of the Foppl-von Karman model for graphene is discussed in [51].

To survey the electronic structure of the proposed device, we use the tight-binding approximation in the framework of the mean-field Hubbard model [52,53], and then utilize coherent transport formalism [52] to calculate the spin-dependent thermocurrent. The Hamiltonian of the system is represented by [52]

$$H = - \sum_{\langle i,j \rangle, \sigma} t'_{ij} c_{i\sigma}^\dagger c_{j\sigma} + U \sum_i (n_{i,\uparrow} \langle n_{i,\downarrow} \rangle + n_{i,\downarrow} \langle n_{i,\uparrow} \rangle - \langle n_{i,\uparrow} \rangle \langle n_{i,\downarrow} \rangle). \quad (1)$$

The first term indicates the tight-binding Hamiltonian of the SZGNR, where  $c_{i\sigma}^\dagger$  and  $c_{j\sigma}$  are the creation and annihilation operators for an electron with the spin index  $\sigma = \uparrow, \downarrow$  at sites  $i$  and  $j$ , respectively.  $t'_{ij}$  in this term is the hopping parameter between the nearest-neighbor atoms at sites  $i$  and  $j$  of the strained system and is a function of atomic bond length  $r$  as [18]

$$t' = t_0 \exp \left[ -\beta \left( \frac{r}{r_0} - 1 \right) \right]. \quad (2)$$

Here,  $t_0 = 2.7$  eV and  $r_0 = 1.42$  Å [18] are the hopping parameter and bond length of unstrained graphene, respectively.  $\beta$  is the decay rate and is assumed to be 4.45 based on first-principles calculations on similar structures in [8], although other values are reported too [18].

The second term in Eq. (1) expresses the e-e Hubbard interaction in the framework of the mean-field approximation.  $U$  is the on-site Coulomb energy assumed to be equal to  $t_0$  [54–56].  $n_{i,\sigma}$  is the particle number operator for an electron with the spin  $\sigma$  at the site  $i$ , and  $\langle n_{i,\sigma} \rangle$  is the mean value of the number operator calculated self-consistently as [57]

$$\begin{aligned} \langle n_{i,\uparrow} \rangle &= \sum_{\uparrow \text{ bands}} \frac{a}{2\pi} \int_{-\pi/a}^{\pi/a} \psi_i^*(\epsilon_k) \psi_i(\epsilon_k) f(\epsilon_k - \mu) dk, \\ \langle n_{i,\downarrow} \rangle &= \sum_{\downarrow \text{ bands}} \frac{a}{2\pi} \int_{-\pi/a}^{\pi/a} \psi_{i+N}^*(\epsilon_k) \psi_{i+N}(\epsilon_k) f(\epsilon_k - \mu) dk, \end{aligned} \quad (3)$$

where  $a$ ,  $N$ , and  $i = 1, \dots, N$  determine the lattice constant, the number of atoms, and the atomic site in the unit cell, respectively. Here, indices  $i$  and  $i + N$  are in regard to wave function components corresponding to spin-up and spin-down, respectively.  $f(\epsilon_k - \mu)$  is the Fermi-Dirac distribution function where  $\mu$  is the chemical potential and  $\epsilon_k$  is the energy in the wave number  $k$ . All band structure calculations are performed at room temperature.  $\psi_\alpha(\epsilon_k)$  is the wave function of the Hamiltonian in Eq. (1) [58]. Consistently, the magnetization at site  $i$  is defined by  $\rho_i = (\langle n_{i,\uparrow} \rangle - \langle n_{i,\downarrow} \rangle)\mu_B$  where  $\mu_B$  is the Bohr magneton.

As concerns matching Bloch wave functions in contacts and the scattering region, we first calculate total transmission and spin transmission by  $T(\epsilon) = \sum_{\alpha=1}^{M_f} \sum_{i=1}^N \psi_{\alpha i}^\dagger \psi_{\alpha i}$  and  $T_s(\epsilon) = \sum_{\alpha=1}^{M_f} \sum_{i=1}^N \psi_{\alpha i}^\dagger \sigma_z \psi_{\alpha i}$ , respectively [57], where  $\psi_{\alpha i}$  is the two-component part of the eigenfunction  $\psi_\alpha$  and  $\sigma_z$  is the  $z$  component of the Pauli matrices. Then, spin-resolved transmission is obtained by  $T_{\uparrow(\downarrow)}(\epsilon) = [T(\epsilon) \pm T_s(\epsilon)]/2$  [57].

Proceeding from the linear response regime, we compute the thermospin current and Seebeck coefficient under applied temperature gradient  $\Delta T$ . The temperature difference between two sides of the strained ZGNR changes the Fermi distribution of the two contacts giving rise to the flow current. The spin-resolved current in Landauer-Büttiker formalism is attained by [59]

$$I_\sigma = \frac{e}{h} \int_{-\infty}^{+\infty} T_\sigma(\epsilon) [f_L(\epsilon, \mu_L, T_L) - f_R(\epsilon, \mu_R, T_R)] d\epsilon, \quad (4)$$

where  $L$  and  $R$  specify left and right contacts. Total charge and spin currents are also obtained by  $I_C = I_\uparrow + I_\downarrow$  and  $I_S = I_\uparrow - I_\downarrow$ , respectively [52].

In the following, we determine the spin-dependent Seebeck coefficient using [52,53]

$$S_\sigma(\mu, T) = -\frac{1}{|e|T} \frac{L_{1\sigma}(\mu, T)}{L_{0\sigma}(\mu, T)}, \quad (5)$$

where intermediate function  $L_{n,\sigma}(\mu, T)$  is defined as

$$L_{n,\sigma}(\mu, T) = -\frac{1}{h} \int_{-\infty}^{+\infty} (\epsilon - \mu)^n \frac{\partial f(\epsilon, \mu, T)}{\partial \epsilon} T_\sigma(\epsilon) d\epsilon.$$

Ultimately, charge and spin Seebeck coefficients are given by  $S_C = (S_\uparrow + S_\downarrow)/2$  and  $S_S = (S_\uparrow - S_\downarrow)$ , respectively [52].

### III. RESULTS AND DISCUSSION

The proposed device in this paper is a ZGNR with a sinusoidal strain across the ribbon. The applied strain induces smaller atomic bond lengths close to the top and bottom of sinusoidal ZGNR rather than middle ones. So the density of atoms around the peaks is higher than the middle region. The ZGNR is along the  $x$  direction and our proposed supercell contains a whole or part of a wavelength that we investigate here. Therefore, the density of atoms along the supercell varies locally, creates nonuniform charge distribution, and induces an electric field [8]. On the other hand, strain gradient can create spatially variable pseudomagnetic field [8,16,60]. These factors give rise to different band structures and hence reveal new transport properties in the system. Indeed, calculations can be based on a strained tight-binding Hamiltonian (as done

here) or on an unstrained one with pseudofields. A comparison between the two calculation methods has been done in [8] and shows similar results.

To proceed further, we added an e-e Hubbard interaction to our sinusoidal SZGNR and found fascinating results. Interestingly, a gap opens, and high spin polarization appears in specific widths of our designed structure in the presence of the e-e interaction. Also, the edge magnetization varies by the strength of strain that we will discuss later. We plot the spin-resolved low-energy spectrum of our SZGNR in Fig. 2 for  $\lambda = 20$  nm,  $h_m = 1$  nm, and widths  $W = \lambda, \lambda/2, \lambda/4$ , and  $\lambda/5$ . These amounts of  $\lambda$  and  $h_m$  create the maximum value of strain 5% in atomic bond lengths of defined strain. Figure 2(a) shows the low-energy band structure of the SZGNR with  $W = \lambda$  in the absence of the Hubbard interaction. As we expect, there is no gap around the Fermi level and no splitting between the two types of spin. This result is similar to reports of previous works on strain in zigzag nanoribbons [27]. The importance of the e-e interaction is revealed in the four diagrams shown in Figs. 2(b)–2(e). A band gap is opened by assuming the existence of the e-e interaction in the system, as seen in Figs. 2(b)–2(e). Figures 2(b) and 2(c) are related to the SZGNR with complete and half wavelength in the width of the ribbon, respectively. In the two later cases, up and down spin states are degenerate due to the same magnitude of strain near two edges of the nanoribbon. It is worth mentioning that if any other nonuniform strain profile induces different stretching around the two edges, spin splitting may occur in the band structure; meanwhile an out-of-plane sinusoidal strain is a choice consistent with experiments [8] and accompanied by more efficient results. Indeed, the A and B sublattices near the two edges have similar bond lengths, and nonuniform strain could not stretch two zigzag edges differently. Therefore, edge magnetization does not change in widths  $W = \lambda, \lambda/2$  by applying sinusoidal strain. These results for edge states are the same as constant strain along the  $y$  direction. Anyway, high spin splitting is observed for the SZGNR with  $W = \lambda/4$  and  $\lambda/5$  in Figs. 2(d) and 2(e). This splitting between spin states is in a way that the bands of one type of spin move upward, while the other type moves downward in the band structure similarly to the spin semiconducting phase. Indeed, by ignoring the interaction between electrons, no gap appears even by applying nonuniform strain in the system.

Our calculation shows that the highest spin polarization occurs for  $W = \lambda/4$ , and it is reduced for larger or smaller widths. This is owing to the most difference between amounts of strain in two edges of the ribbon. Each atomic sublattice near two edges of the ribbon experiences a different strain that causes spin-polarized edge states. Experimentally, periodic ripples with various wavelengths from 2 nm to several tens of nanometers are observed in the graphene sheet [61]. However, here we investigated sinusoidal modulation across the nanoribbon. Moreover, when  $W = \lambda$  energy bands of spin-up and spin-down are degenerate, while  $W = \lambda/4$  corresponds to the highest spin polarization, so  $W = N(\lambda + \lambda/4)$  could cause approximately the same behavior in the band structure with  $N = 1, 2, \dots$ . This can also be used in experiment.

Furthermore, if an in-plane strain is taken into account similar to [8], the bond lengths near the edge located at the crest

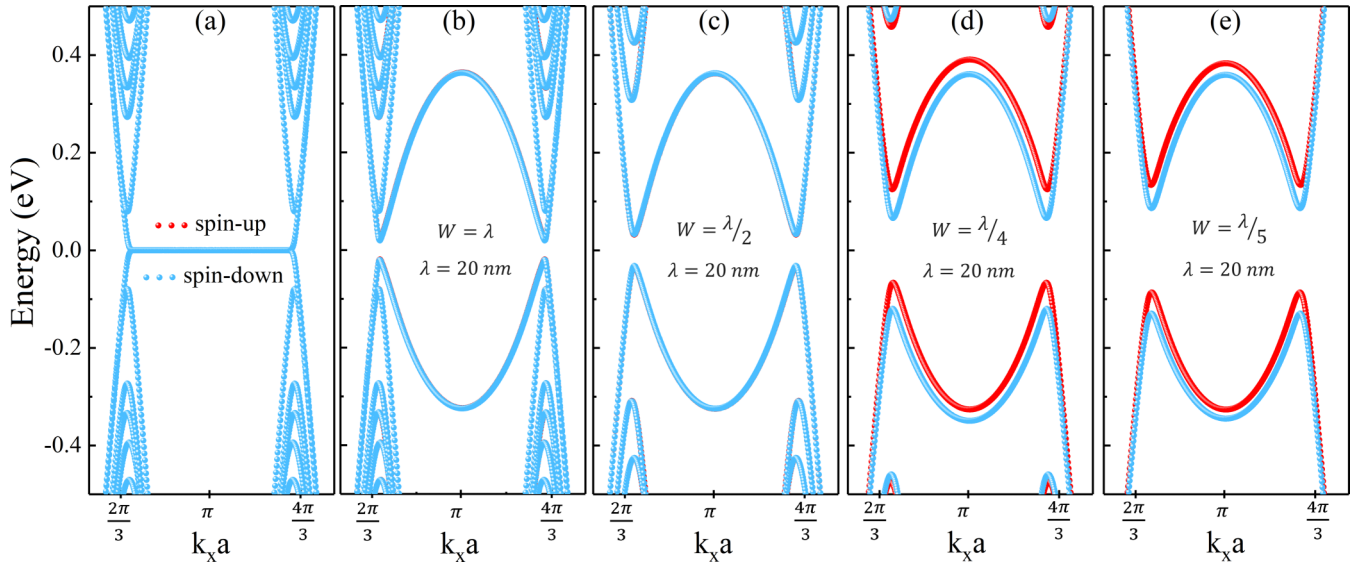


FIG. 2. Low-energy band structure of SZGNR with zero Hubbard interaction in (a) width  $W = \lambda$  and nonzero Hubbard interaction in (b)  $W = \lambda$ , (c)  $W = \lambda/2$ , (d)  $W = \lambda/4$ , (e)  $W = \lambda/5$ . Here,  $\lambda = 20$  nm,  $h_m = 1$  nm equivalent to maximum strain  $\epsilon = 5\%$ .

would be larger than the other edge when  $W = \lambda/4$ . So again, different strain profiles near the edges lead to the spin splitting in the band structure. Anyway, such nonuniform strain could induce remarkable spin splitting, although the spin polarization usually happens by applying an electric or magnetic field on the system [62,63]. For example, the in-plane transverse electric field induces different spin-dependent band gaps for two types of spin [62,64]. However, in our defined structure, spin-dependent bands move oppositely in the edge band structure. Hence, their band gap is the same, approximately. Furthermore, by comparing Fig. 2(b) to Fig. 2(e), it has been found that the spin gap is increased by decreasing the width of the SZGNR from  $W = \lambda$  to  $W = \lambda/5$  in a particular wavelength. Therefore, the e-e interaction with inhomogeneous

strain in the ZGNR generates a spin semiconductor phase with a tunable spin-dependent band gap.

For more clarification, we plot the low-energy band structure of the SZGNR for different sets of  $W$  and  $\lambda$  in Fig. 3. Figures 3(a)–3(c) besides Fig. 2(b) correspond to a given width  $W = 20$  nm and maximum strain  $\epsilon = 5\%$  but different values of  $\lambda$ . Figures 3(d) and 3(e) are in regard to the different strain wavelengths when  $W = \lambda/4$  and  $\epsilon = 5\%$ . Figures 3(b), 3(d) and 3(e) along with Fig. 2(d) show slight increase in spin splitting of the band structure by enhancing  $\lambda$  when the maximum strain is constant  $\epsilon = 5\%$  and  $W = \lambda/4$ . On the other hand, these band structures illustrate the effect of the SZGNR width in constant strain when  $W = \lambda/4$ . Here, increasing the ribbon width is equivalent to increasing the

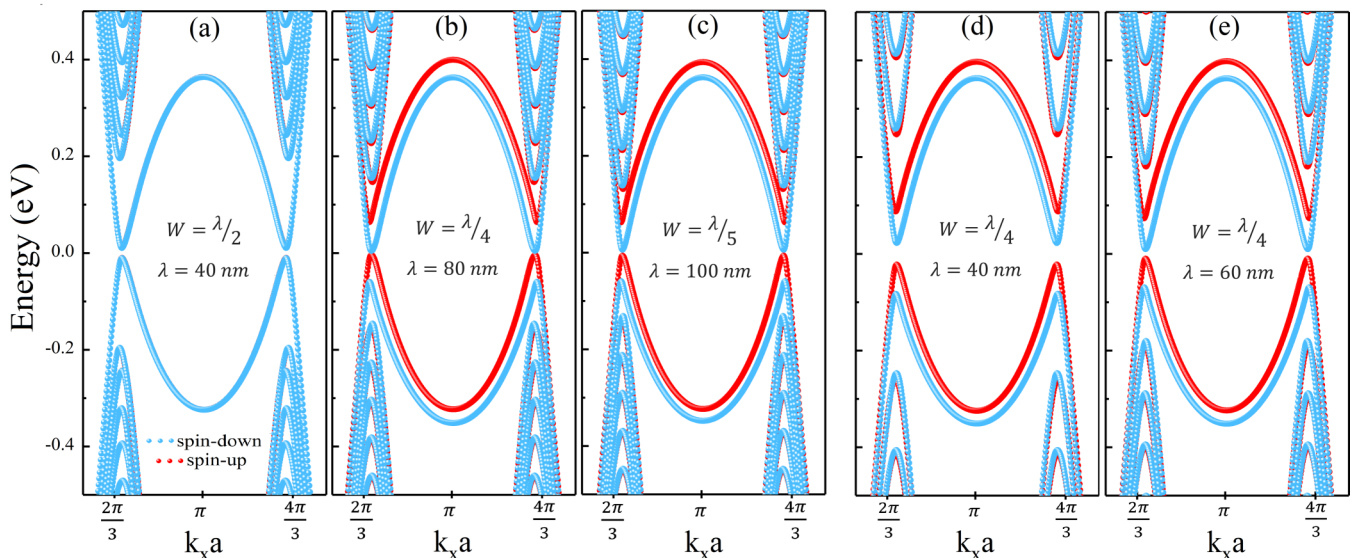


FIG. 3. (a)–(c) Low-energy band structures of SZGNR with indicated values of  $\lambda$  and for given ribbon width  $W = 20$  nm and  $\epsilon = 5\%$ . They correspond to  $h_m = 2, 4, 5$  nm, respectively. (d), (e) Band structure of SZGNR with different ribbon widths and strain wavelengths when  $W = \lambda/4$  and  $\epsilon = 5\%$ , corresponding to  $h_m = 2, 3$  nm, respectively. In all parts  $U = t_0$ .

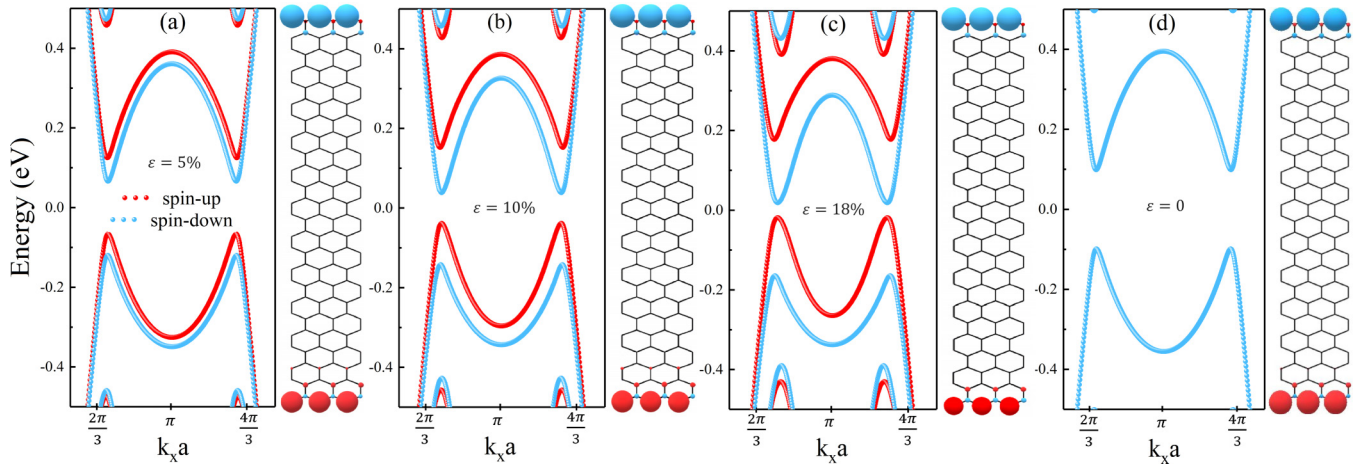


FIG. 4. The effect of strain magnitude on low-energy band structure of SZGNR and corresponding magnetizations with  $\lambda = 20$  nm, width  $W = \lambda/4$ , and  $U = t_0$ . (a) Maximum strain  $\varepsilon = 5\%$ , (b)  $\varepsilon = 10\%$ , (c)  $\varepsilon = 18\%$ , and (d)  $\varepsilon = 0$ . They are corresponding to equivalent values  $h_m = 1$  nm,  $h_m = 1.5$  nm,  $h_m = 2$  nm, and  $h_m = 0$ , respectively.

strain wavelength and leads to less band gap. Indeed, reducing the ribbon width enhances the coupling between edge states, or in other words raises the e-e interaction effect [65]. This effect also occurs in other sets of  $W$  and  $\lambda$  that can be seen by comparing plots Fig. 2(c) and Fig. 3(a) for  $W = \lambda/2$  or Fig. 2(e) and Fig. 3(c) for  $W = \lambda/5$ . In the rest of this paper, we perform our calculation on the case of  $W = \lambda/4$  due to its most spin polarization compared to other widths of SZGNRs. We investigate the low-energy band structure and spin magnetization of the designed system under different magnitudes of strain in the following. To this purpose, we assume  $\lambda = 20$  nm and  $W = \lambda/4$  in the SZGNR. Figure 4 shows the effect of increasing strain on edge states. First, we apply the sinusoidal strain with  $h_m = 1$  nm in Fig. 4(a), which produces maximum strain  $\varepsilon = 5\%$  in bond lengths. As seen, the spin degeneracy is broken in the presence of our defined nonuniform strain and Hubbard interaction. Besides, the two edges show different magnetization, and therefore the system exhibits a small spin polarization. The changes are in a way that one edge shows larger magnetization rather than another one. The spin density decays from the ribbon's edges to the middle, and the edges have more contribution relative to the bulk.

Second, by increasing maximum strain in bond lengths to  $\varepsilon = 10\%$  (this is equivalent to  $h_m = 1.5$  nm) in Fig. 4(b),

spin polarization is enhanced. In contrast, the spin band gap decreases. Then, we raise the strain to  $\varepsilon = 18\%$  and see similar changes to those seen in Fig. 4(c). Again, the spin gap decreased, and spin polarization increases. Also, a substantial difference between the spin distribution of two edges, about  $\delta\rho = 0.06\mu_B$ , is observed in the case of Fig. 4(c) where  $\rho = 0.26\mu_B$  at the upper edge that is related to down spins. This difference for Figs. 4(a) and 4(b) is  $\delta\rho = 0.02\mu_B$  and  $\delta\rho = 0.04\mu_B$ , respectively. Ultimately, we plot the edge states of the ZGNR with  $W = 5$  nm in the absence of strain in Fig. 4(d). As we expected there is no spin polarization in this case. As a result, the defined strain profile could induce spin splitting and finite magnetization in SZGNRs. Also, comparing magnetization in panels (a)–(c) in Fig. 4 shows that there is more variation of edge polarization in the higher values of strain. So, enhancing strain could increase the magnetic effects of the system and decreases the band gap.

To progress further, we apply a thermal gradient between two sides of our designed SZGNR in this section to study the thermoelectric current and Seebeck effect. The proposed structure for this purpose is the SZGNR with  $\lambda = 20$  nm and  $W = \lambda/4$  with the three strain values given in Figs. 4(a)–4(c). The corresponding spin-polarized thermocurrents are plotted in Fig. 5 as a function of temperature. Interestingly, the pure

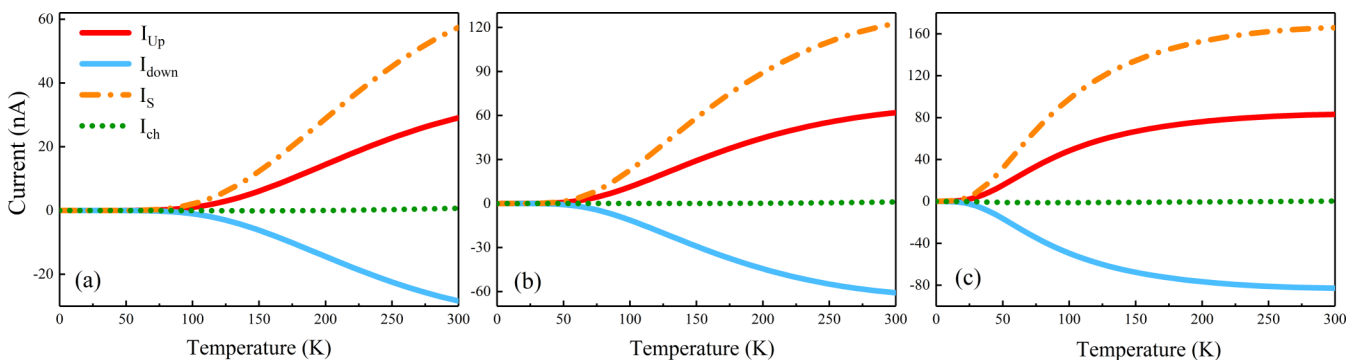


FIG. 5. Spin-resolved, charge, and spin currents in SZGNR with  $\lambda = 20$  nm, width  $W = \lambda/4$ , and  $U = t_0$  for (a)  $\varepsilon = 5\%$ , (b)  $\varepsilon = 10\%$ , and (c)  $\varepsilon = 18\%$ , under applied  $\Delta T = 20$  K. The currents are in regard to the band structures of panels (a)–(c) in Fig. 4, respectively.

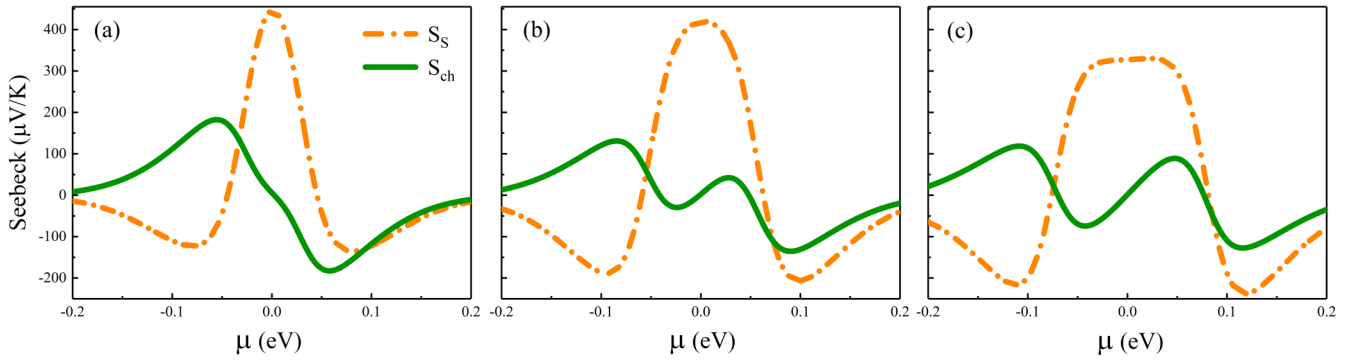


FIG. 6. Charge and spin Seebeck coefficient against chemical potential in SZGNR with  $\lambda = 20$  nm,  $W = \lambda/4$ , and  $U = t_0$  for (a)  $\epsilon = 5\%$ , (b)  $\epsilon = 10\%$ , and (c)  $\epsilon = 18\%$  under applied  $\Delta T = 20$  K. The currents are in regard to the band structures of panels (a)–(c) in Fig. 4, respectively.

spin current is found in a wide range of temperatures for these three systems with different strain values. The band structure is symmetric for inversion of electrons and holes in the energy window around the Fermi energy corresponding to the considered temperatures. Here, the parts of bands that participate in the current show symmetry features. This energy range is about  $-0.25$  eV to  $0.25$  eV at  $T = 300$  K by considering the variation of the Fermi-Dirac distribution. As seen in Fig. 5(a), in the case of  $\epsilon = 5\%$  up and down spin currents appear from  $T = 60$  K and have the same magnitude and opposite directions to 300 K in temperature difference  $\Delta T = 20$  K. This leads to zero charge current and also a high spin current that flows from left to right of the sample. At room temperature, the induced pure thermospin current reaches 60 nA. Here, spin-up carriers are holes that flow from left to right, and electrons carry spin-down that move inversely. They are equal, so there is no net charge current in the system. By increasing the strain in Figs. 5(b) and 5(c), we observe that a pure spin current exists, and it begins in lower temperatures. Smaller band gaps around the Fermi level could produce current at lower temperatures. This is owing to the existence of involved bands in low temperatures (due to the effect of Fermi distribution). Figure 5(c) shows that pure spin current goes up to 160 nA at room temperature. Generally, by increasing the strain's strength, the spin gap decreases, and therefore the spin current increases. This magnitude is more than ten times larger than previous works on GNRs and carbon nanotubes with vacancy [59,66].

Figure 6 shows spin and charge Seebeck coefficients against chemical potential  $\mu$  at  $T = 300$  K corresponding to band structures in Fig. 4, respectively. In all strains, the spin Seebeck coefficient has a peak at  $\mu = 0$ , while the charge Seebeck is zero at this point. This peak is sharper and has a larger value for cases with a higher strain than seen in Figs. 6(a)–6(c). This peak for the case of  $\epsilon = 5\%$  has the value  $S_S = 450$   $\mu\text{V/K}$  that is relatively large and comparable to other reported values for ZGNRs [67–69] and carbon chains

[53]. The value of the spin Seebeck is dependent on the energy gap, and by increasing the strength of the strain, the spin gap decreases, and therefore the spin Seebeck slightly decreases, but the flat plateau increases. In this regard, the SZGNR with  $\epsilon = 18\%$  shows an approximately flat plateau around  $\mu = 0$  similarly to armchair and zigzag graphene nanoribbons with structural defects [59,66]. Moreover, by increasing or decreasing the chemical potential,  $S_S$  is reduced and  $S_C$  has nonvanishing values.

#### IV. CONCLUSION

In summary, we applied a sinusoidal-shaped inhomogeneous strain across a zigzag edge graphene nanoribbon. We described its effect on the low-energy band structure of the GNR using the tight-binding method and mean-field Kane-Mele Hubbard model. Then we calculated the thermoelectric properties of the GNR in the presence of a temperature gradient in the framework of the linear response regime. The results showed that the simultaneous presence of Hubbard interaction and nonuniform strain (that are barely considered in studies) in the GNR could lift the spin degeneracy and produce spin-semiconducting behavior with a tunable spin gap. Generally, for creating the spin effect by strain, the nonuniform strain could induce different effects on both edges of the zigzag nanoribbon. In detail, two different sublattices near the zigzag edges feel different strains that cause a spin filtering effect in the presence of e-e interaction. Furthermore, as we expect, the larger strain produces higher spin polarization and, finally, higher values for spin current. Therefore, the SZGNR exhibits spin-up and spin-down currents with opposite flow directions and, therefore, pure spin current in a wide range of temperatures. Besides, high values of the spin current and Seebeck coefficient are found at room temperature, even in low values of strain compared to other reported values for ZGNRs. These findings will be useful for designing stretchable electronics and spin-based thermoelectric devices.

[1] E. Han, J. Yu, E. Annevelink, J. Son, D. A. Kang, K. Watanabe, T. Taniguchi, E. Ertekin, P. Y. Huang, and A. M. van der Zande, *Nat. Mater.* **19**, 305 (2020).

[2] B. Amorim, A. Cortijo, F. De Juan, A. Grushin, F. Guinea, A. Gutiérrez-Rubio, H. Ochoa, V. Parente, R. Roldán, P. San-Jose *et al.*, *Phys. Rep.* **617**, 1 (2016).

- [3] G. G. Naumis, S. Barraza-Lopez, M. Oliva-Leyva, and H. Terrones, *Rep. Prog. Phys.* **80**, 096501 (2017).
- [4] C. Si, Z. Sun, and F. Liu, *Nanoscale* **8**, 3207 (2016).
- [5] Z. Dai, L. Liu, and Z. Zhang, *Adv. Mater.* **31**, 1805417 (2019).
- [6] D. Midtvedt, C. H. Lewenkopf, and A. Croy, *2D Mater.* **3**, 011005 (2016).
- [7] S. Deng, A. V. Sumant, and V. Berry, *Nano Today* **22**, 14 (2018).
- [8] R. Banerjee, V.-H. Nguyen, T. Granzier-Nakajima, L. Pabbi, A. Lherbier, A. R. Binion, J.-C. Charlier, M. Terrones, and E. W. Hudson, *Nano Lett.* **20**, 3113 (2020).
- [9] S. T. Gill, J. H. Hinnefeld, S. Zhu, W. J. Swanson, T. Li, and N. Mason, *ACS Nano* **9**, 5799 (2015).
- [10] C. Lee, X. Wei, J. W. Kysar, and J. Hone, *Science* **321**, 385 (2008).
- [11] R. Gupta, F. Rost, M. Fleischmann, S. Sharma, and S. Shallcross, *Phys. Rev. B* **99**, 125407 (2019).
- [12] T. Fujita, M. Jalil, and S. Tan, *Appl. Phys. Lett.* **97**, 043508 (2010).
- [13] S. Souma, M. Ueyama, and M. Ogawa, *Appl. Phys. Lett.* **104**, 213505 (2014).
- [14] F. Guinea, M. I. Katsnelson, and M. A. H. Vozmediano, *Phys. Rev. B* **77**, 075422 (2008).
- [15] N. Levy, S. Burke, K. Meaker, M. Panlasigui, A. Zettl, F. Guinea, A. C. Neto, and M. F. Crommie, *Science* **329**, 544 (2010).
- [16] T. Low and F. Guinea, *Nano Lett.* **10**, 3551 (2010).
- [17] S. M. Choi, S. H. Jhi, and Y. W. Son, *Phys. Rev. B* **81**, 081407(R) (2010).
- [18] V. M. Pereira, A. H. Castro Neto, and N. M. R. Peres, *Phys. Rev. B* **80**, 045401 (2009).
- [19] Y. Lu and J. Guo, *Nano Res.* **3**, 189 (2010).
- [20] Z. H. Ni, T. Yu, Y. H. Lu, Y. Y. Wang, Y. P. Feng, and Z. X. Shen, *ACS Nano* **2**, 2301 (2008).
- [21] Y. Chang, T. Albash, and S. Haas, *Phys. Rev. B* **86**, 125402 (2012).
- [22] F. Guinea, M. Katsnelson, and A. Geim, *Nat. Phys.* **6**, 30 (2010).
- [23] E. Santos, S. Riikonen, D. Sánchez-Portal, and A. Ayuela, *J. Phys. Chem. C* **116**, 7602 (2012).
- [24] L. Kou, C. Tang, W. Guo, and C. Chen, *ACS Nano* **5**, 1012 (2011).
- [25] T. Ma, F. Hu, Z. Huang, and H.-Q. Lin, *Appl. Phys. Lett.* **97**, 112504 (2010).
- [26] J. Viana-Gomes, V. M. Pereira, and N.M.R. Peres, *Phys. Rev. B* **80**, 245436 (2009).
- [27] G. Yang, B. Li, W. Zhang, M. Ye, and T. Ma, *J. Phys.: Condens. Matter* **29**, 365601 (2017).
- [28] S. Cheng, J. Yu, T. Ma, and N. M. R. Peres, *Phys. Rev. B* **91**, 075410 (2015).
- [29] J. S. Nascimento, D. R. da Costa, M. Zarenia, A. Chaves, and J. M. Pereira, Jr., *Phys. Rev. B* **96**, 115428 (2017).
- [30] G. S. Diniz, M. R. Guassi, and F. Qu, *J. Appl. Phys.* **116**, 113705 (2014).
- [31] A. C. McRae, G. Wei, and A. R. Champagne, *Phys. Rev. Applied* **11**, 054019 (2019).
- [32] N. Wei, L. Xu, H.-Q. Wang, and J.-C. Zheng, *Nanotechnology* **22**, 105705 (2011).
- [33] L. Lindsay, W. Li, J. Carrete, N. Mingo, D. A. Broido, and T. L. Reinecke, *Phys. Rev. B* **89**, 155426 (2014).
- [34] P. S. E. Yeo, K. P. Loh, and C. K. Gan, *Nanotechnology* **23**, 495702 (2012).
- [35] G. Cocco, E. Cadelano, and L. Colombo, *Phys. Rev. B* **81**, 241412(R) (2010).
- [36] G. Gui, D. Morgan, J. Booske, J. Zhong, and Z. Ma, *Appl. Phys. Lett.* **106**, 053113 (2015).
- [37] P. S. E. Yeo, M. B. Sullivan, K. P. Loh, and C. K. Gan, *J. Mater. Chem. A* **1**, 10762 (2013).
- [38] A. Mani and C. Benjamin, *Phys. Rev. E* **96**, 032118 (2017).
- [39] A. Mani, S. Pal, and C. Benjamin, *Sci. Rep.* **9**, 6018 (2019).
- [40] K. H. Park and U. Ravaioli, *J. Appl. Phys.* **122**, 025115 (2017).
- [41] W. Bao, F. Miao, Z. Chen, H. Zhang, W. Jang, C. Dames, and C. N. Lau, *Nat. Nanotechnol.* **4**, 562 (2009).
- [42] F. Schedin, A. K. Geim, S. V. Morozov, E. Hill, P. Blake, M. Katsnelson, and K. S. Novoselov, *Nat. Mater.* **6**, 652 (2007).
- [43] H. Hu, X. Guo, D. Hu, Z. Sun, X. Yang, and Q. Dai, *Adv. Sci.* **5**, 1800175 (2018).
- [44] B. Javvaji, B. Mortazavi, T. Rabczuk, and X. Zhuang, *Nanoscale Adv.* **2**, 3394 (2020).
- [45] L. Tapasztó, T. Dumitrică, S. J. Kim, P. Nemes-Incze, C. Hwang, and L. P. Biró, *Nat. Phys.* **8**, 739 (2012).
- [46] Y. Wei, B. Wang, J. Wu, R. Yang, and M. L. Dunn, *Nano Lett.* **13**, 26 (2013).
- [47] C. Androulidakis, E. N. Koukaras, K. Sampathkumar, J. Rahova, C. Galiotis, and O. Frank, *Extreme Mech. Lett.* **40**, 100948 (2020).
- [48] M. Fujita, K. Wakabayashi, K. Nakada, and K. Kusakabe, *J. Phys. Soc. Jpn.* **65**, 1920 (1996).
- [49] C. Davini, A. Favata, and R. Paroni, *Int. J. Non-Linear Mech.* **116**, 281 (2019).
- [50] M. Lewicka, L. Mahadevan, and M. R. Pakzad, *Proc. R. Soc. London, Ser. A* **467**, 402 (2011).
- [51] A. Pacheco-Sanjuán and R. Batra, *Int. J. Mech. Sci.* **163**, 105154 (2019).
- [52] M. Shirdel-Havar and R. Farghadan, *Phys. Rev. B* **97**, 235421 (2018).
- [53] F. Ildarabadi and R. Farghadan, *J. Magn. Magn. Mater.* **497**, 165980 (2020).
- [54] J. L. Lado and J. Fernández-Rossier, *Phys. Rev. Lett.* **113**, 027203 (2014).
- [55] S. Krompiewski and G. Cuniberti, *Phys. Rev. B* **96**, 155447 (2017).
- [56] O. V. Yazyev, *Phys. Rev. Lett.* **101**, 037203 (2008).
- [57] M. Wierzbicki, J. Barnaś, and R. Swirkowicz, *J. Phys.: Condens. Matter* **27**, 485301 (2015).
- [58] M. Wierzbicki, J. Barnaś, and R. Swirkowicz, *Phys. Rev. B* **91**, 165417 (2015).
- [59] M. Shirdel-Havar and R. Farghadan, *Phys. Chem. Chem. Phys.* **20**, 16853 (2018).
- [60] M. R. Masir, D. Moldovan, and F. Peeters, *Solid State Commun.* **175**, 76 (2013).
- [61] K.-K. Bai, Y. Zhou, H. Zheng, L. Meng, H. Peng, Z. Liu, J.-C. Nie, and L. He, *Phys. Rev. Lett.* **113**, 086102 (2014).
- [62] E.-J. Kan, Z. Li, J. Yang, and J. Hou, *Appl. Phys. Lett.* **91**, 243116 (2007).
- [63] E. H. Hwang and S. Das Sarma, *Phys. Rev. B* **80**, 075417 (2009).
- [64] S. Zamani and R. Farghadan, *Phys. Rev. Applied* **10**, 034059 (2018).

- [65] G. Z. Magda, X. Jin, I. Hagymási, P. Vancsó, Z. Osváth, P. Nemes-Incze, C. Hwang, L. P. Biro, and L. Tapasztó, *Nature (London)* **514**, 608 (2014).
- [66] M. Shirdel-Havar and R. Farghadan, *J. Phys. Chem. C* **123**, 20105 (2019).
- [67] J. Li, B. Wang, F. Xu, Y. Wei, and J. Wang, *Phys. Rev. B* **93**, 195426 (2016).
- [68] M. Zeng, W. Huang, and G. Liang, *Nanoscale* **5**, 200 (2013).
- [69] B. Zhou, B. Zhou, Y. Zeng, G. Zhou, and T. Ouyang, *J. Appl. Phys.* **117**, 104305 (2015).